Photon-Sail Equilibria in the Alpha Centauri System

Heiligers, M.J.; Schoutetens, F.R.J.; Dachwald, Bernd

Important note
To cite this publication, please use the final published version (if applicable).
Please check the document version above.

Photon-Sail Equilibria in the Alpha-Centauri System

Jeannette Heiligers [*] and Frederic Schoutetens [†]
Delft University of Technology, 2629 HS, Delft, The Netherlands

Bernd Dachwald [‡]
FH Aachen University of Applied Sciences, Aachen, Germany

I. Introduction

Our closest neighboring star system, Alpha Centauri, is located at a "mere" 275,000 astronomical units (au) from Earth. Due to its "close proximity" to Earth, Alpha Centauri is often considered as the prime target for a future interstellar exploration mission [1]. It holds significant scientific importance for better understanding our Sun, and stars in general, and for advancing our knowledge on the formation and evolution of the Solar System [2]. Moreover, by visiting Alpha Centauri, Earth-like exoplanets may be discovered (in addition to the discovery of Proxima Centauri b in 2016 [3]). Voyager 1, our fastest and farthest spacecraft, 146 au from the Sun at the time of writing, would take approximately 75,000 years to reach Alpha Centauri. Photon-sail propulsion could substantially reduce this travel time [4] even though it exclusively makes use of the radiation pressure from a star to drive the spacecraft forward [5]. This novel propulsion technology has made significant technological progress in recent years through JAXA's IKAROS mission, NASA's NanoSail-D2 mission and the LightSail-1 and LightSail-2 missions by the Planetary Society. Continued technological advancement will be achieved through other proposed and scheduled missions such as NASA's NEA Scout mission [6]. Proposals for using photon sails to reach targets far beyond our Solar System are not new, see for example References [4, 7], and initiatives with clear goals of reaching Alpha Centauri within a generation are underway, e.g., the Breakthrough Starshot project[*]. However, little is known about the dynamics of the photon sail once it arrives in the other star system, especially in a multi-star system like Alpha Centauri. To date, the only works investigating these dynamics include References [8] and [9]. Both articles focussed on the dynamics in the binary-star system composed of the stars Alpha Centauri A and B, and investigated the possibility of decelerating the spacecraft after arrival, assuming a graphene-based sail covered with a highly reflective coating. The MIRA Collaboration focused on the computation of artificial equilibria (AE) in the same binary-star system, but for a photon-balloon spacecraft, before investigating capture and transfer trajectories for a photon-sail propelled spacecraft in the elliptical restricted three-body problem (ER3BP) [2, 10].

[*]Assistant Professor, Faculty of Aerospace Engineering, M.J.Heiligers@tudelft.nl
[†]Graduate Student, Faculty of Aerospace Engineering, Frederic.Schoutetens@community.isunet.edu
[‡]Professor, FH Aachen University of Applied Sciences, Dachwald@fh-aachen.de
[*]Breakthrough Starshot, `https://breakthroughinitiatives.org/initiative/3` [retrieved April 20, 2020]

Building on the works mentioned, this Note examines, for the first time, the photon-sail artificial equilibria in the ER3BP under the effect of two radiative source, with application to the Alpha-Centauri system. As such, it is different from the work in Reference [10] as this Note considers a photon sail instead of photon balloon. The current work also distinguishes itself from the computation of AE in our own Solar System (either in the circular or elliptical restricted three-body problem [5, 11–14]) due to the presence of two radiative sources. In order to compute and analyze the photon-sail AE in the binary star system, this Notes derives a new photon-sail acceleration model for both a one-sided and two-sided photon sail, where a two-sided photon sail is assumed to have a reflective coating on both sides of the sail membrane. Instead, a one-sided photon sail has a highly emissive coating on the back for thermal control, which prevents the backside of the sail to be exposed to either of the two stars. With the new acceleration model in place, the AE are presented and demonstrated to be very different from those found under the effect of a single radiating source. The AE are subsequently analyzed for their stability and previously unknown regions of (in)stability in the Alpha-Centauri system are identified. As a final novel contribution, this Note investigates heteroclinic-like connections between the newly found equilibria. Again, while photon-sail heteroclinic-like connections have been investigated within our own single-star Solar System [15–17], the search for such transfers under the effect of two radiative stars is new and allows further insights in the dynamics and maneuverability of a photon-sail in a two-radiative ER3BP such as that of the Alpha Centauri system.

II. Alpha Centauri

Alpha Centauri is a triple-star system, consisting of the stars Alpha Centauri A, B, and C (hereafter in short referred to as α-Cen A, α-Cen B, and α-Cen C), where α-Cen A and α-Cen B form the binary-star system α-Cen AB. A schematic of the Alpha-Centauri system is shown in Fig. 1. The stars of the α-Cen AB system are Sun-like, though α-Cen A is larger and more luminous than the Sun, while α-Cen B is smaller and cooler than our Sun, see Table 1 that provides the radii, masses and luminosities of the three stars expressed in solar units. α-Cen C (officially termed Proxima Centauri) is the smallest and faintest of the triple-star system [18]. In its habitable zone, an Earth-sized exoplanet, Proxima Centauri b, was discovered in 2016 [3], which is the prime target of the Breakthrough Starshot project. Though of significant scientific interest, this Note is mainly concerned with the photon-sail dynamics in the α-Cen AB binary system (note that, from here on, the prefix "binary" will be omitted for brevity). Because of the far distance of α-Cen C from the α-Cen AB system, its gravitational and stellar radiation pressure effect on the photon-sail dynamics in α-Cen AB is neglected in this Note (e.g., the radiation pressure is in the order of 10^{-17} N/m^2). To describe the orbital configuration of the α-Cen AB system, the so-called observer reference frame $O_{\mathcal{A}}(\hat{\mathbf{x}}_{O,A}, \hat{\mathbf{y}}_{O,A}, \hat{\mathbf{z}}_{O,A})$ centered at α-Cen A is introduced, see Fig. 2. The direction of $\hat{\mathbf{z}}_{O,A}$ is defined towards Earth and the plane perpendicular to $\hat{\mathbf{z}}_{O,A}$ is referred to as the "plane of the sky" or the "apparent orbital plane". Both $\hat{\mathbf{x}}_{O,A}$ and $\hat{\mathbf{y}}_{O,A}$ are confined to this plane, where $\hat{\mathbf{x}}_{O,A}$ points north and the direction of $\hat{\mathbf{y}}_{O,A}$ completes the right-handed reference frame. In this reference frame,
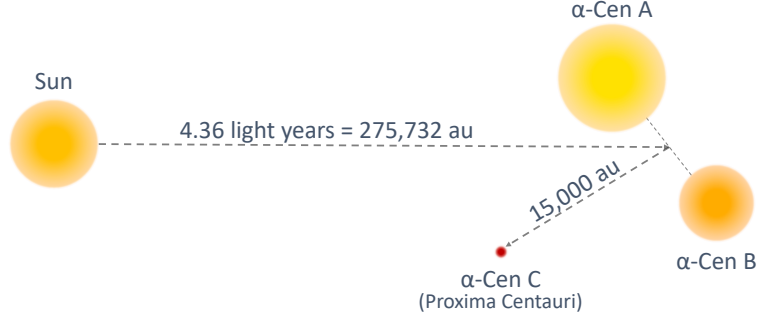
Fig. 1   Schematic of the Alpha-Centauri system (distances not to scale, size of stars to scale).

Table 1   Radius, mass, and luminosity of the stars of the Alpha-Centauri system.

Star	Radius, $R_\odot$	Mass, $M_\odot$	Luminosity, $L_\odot$
α-Cen A	1.2234^a	1.1055^a	1.519^b
α-Cen B	0.8632^a	0.9373^a	0.5002^b
α-Cen C	0.1542^a	0.1221^a	0.0015^c

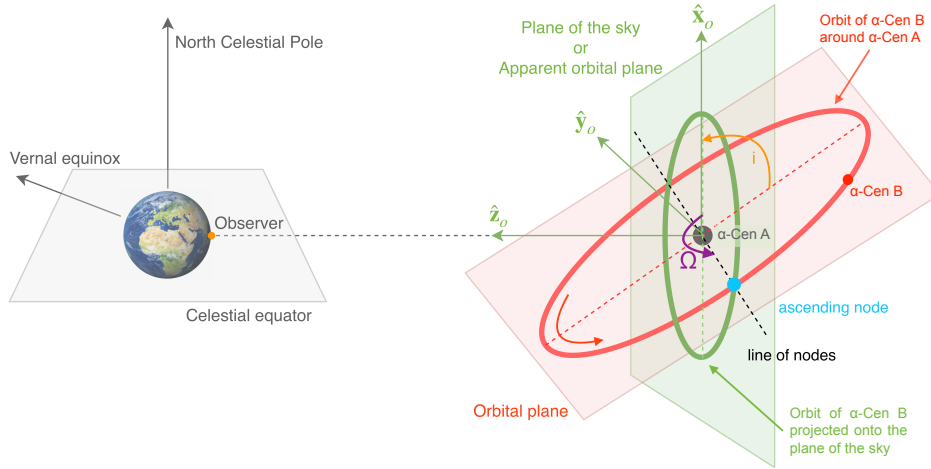Notes: [a] from [18], [b] from [21], [c] from [3].

Fig. 2   Schematic of the observer reference frame $\mathcal{O}_\mathcal{A}$, the orbit of α-Cen B around α-Cen A (red orbit), and the orbit of α-Cen B projected onto the plane of the sky (green orbit).

the orbital elements of the secondary star, α-Cen B, around the primary star, α-Cen A, are determined as in Table 2. Note that the longitude of the ascending node, Ω, is measured eastward from $\hat{x}_{O,A}$, as illustrated by the purple arrow in Fig. 2, and that the ascending node is defined as the node where the secondary star moves away from the observer with respect to the plane of the sky, as depicted with the blue dot in Fig. 2 [19]. Furthermore, the inclination, i, is defined as the angle from the orbital plane to the plane of the sky, depicted by the orange arrow in Fig. 2 [20]. The orbit of α-Cen B around α-Cen A projected onto the plane of the sky (and thus as seen from Earth) is shown in Fig. 3a, where the star's positions at the indicated years are depicted with blue dots.

3

Table 2   Orbital elements of α-Cen B about α-Cen A in frame $O_{\mathcal{A}}$ [22].

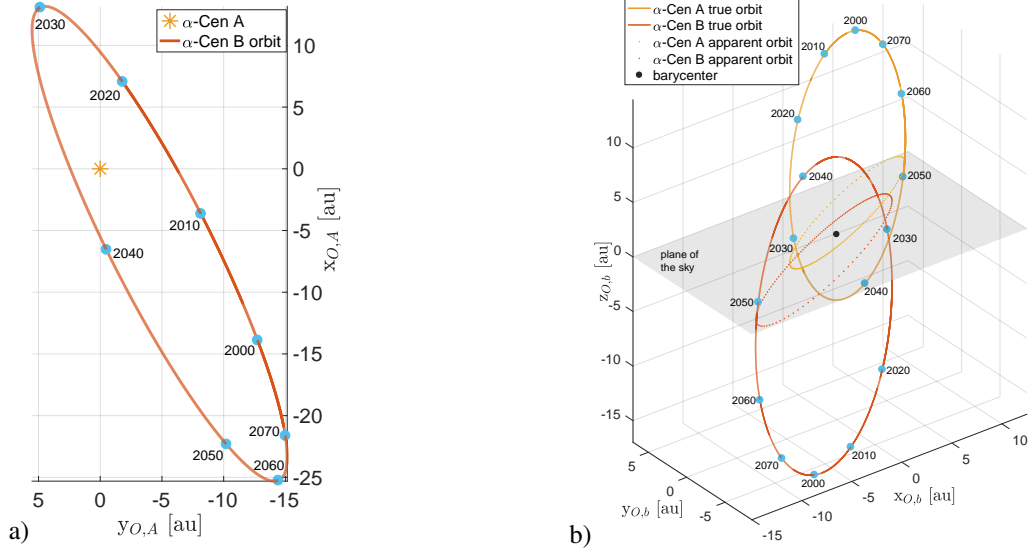| Parameter	Unit	Value
Semi-major axis a	au	23.517
Eccentricity e	-	0.5208
Inclination i	deg	79.320
Longitude of ascending node Ω	deg	205.064
Argument of periapsis ω	deg	232.006
Orbital period T	yr	79.929

Fig. 3   Orbital representations of the α-Cen AB system. a) In frame $O_{\mathcal{A}}$, b) in frame O_b.

Instead of describing the orbital configuration through the motion of α-Cen B around α-Cen A, the mass distribution of the two stars can be used to obtain the semi-major axes of the motion of both stars around their barycenter as $a_A = \frac{M_B}{M_A + M_B} a$ and $a_B = \frac{M_A}{M_A + M_B} a$, where M is the stellar mass and subscripts A and B refer to α-Cen A and α-Cen B, respectively. Inserting the values of Table 1 and Table 2 into these expressions results in semi-major axes of 10.790 au and 12.726 au for α-Cen A and B, respectively. Their distance at closest approach is 11.3 au, similar to the distance between Saturn and the Sun, whereas their largest separation is 35.8 au, similar to the distance between Neptune and the Sun. Due to conservation of angular momentum, both orbits have the same eccentricity, $e_A = e_B = e = 0.5208$, as well as the same inclination, $i_A = i_B = i = 79.320$ deg (defined in frame $O_{\mathcal{A}}$). However, their argument of periapsis differs by 180°. Figure 3b provides a three-dimensional view of the motion of the stars in a reference frame $O_b(\hat{\mathbf{x}}_{O,b}, \hat{\mathbf{y}}_{O,b}, \hat{\mathbf{z}}_{O,b})$, similar to $O_{\mathcal{A}}$ but shifted to the system's barycenter. The figure includes the projection of the orbits of α-Cen A and B onto the plane of the sky.
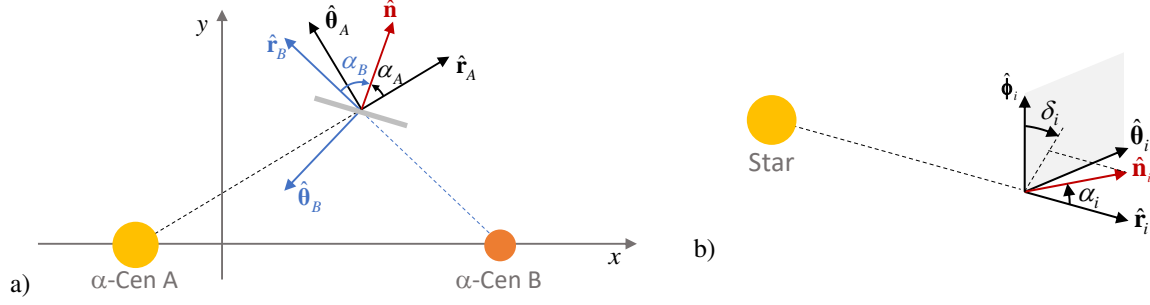
Fig. 4   a) Schematic of the photon-pressure augmented ER3BP and frames $\mathcal{P}$, $\mathcal{A}$, and $\mathcal{B}$, b) definition of the cone and clock angles.

III. Dynamical System

The orbital dynamics of a photon-sail spacecraft in the α-Cen AB system will be investigated within the dynamical framework of the photon-pressure augmented restricted three-body problem, particularly the elliptic restricted three-body problem (ERTBP) [23] to account for the large eccentricity of the α-Cen AB system.

A. Photon-Pressure Augmented Elliptical Restricted Three-Body Problem

The equations of motion of the photon sail in the ERTBP are defined in a pulsating synodic reference frame $\mathcal{P}(\hat{\mathbf{x}}, \hat{\mathbf{y}}, \hat{\mathbf{z}})$, where the direction of $\hat{\mathbf{x}}$ is along the line connecting α-Cen A and B, pointing towards α-Cen B, $\hat{\mathbf{z}}$ is oriented along the angular momentum vector of the α-Cen AB system, and the direction of $\hat{\mathbf{y}}$ completes the right-handed reference frame, see Fig. 4 (the other frames depicted in Fig. 4, i.e., frames $\mathcal{A}(\hat{\mathbf{r}}_A, \hat{\boldsymbol{\theta}}_A, \hat{\boldsymbol{\phi}}_A)$ and $\mathcal{B}(\hat{\mathbf{r}}_B, \hat{\boldsymbol{\theta}}_B, \hat{\boldsymbol{\phi}}_B)$ as well as the unit vector $\hat{\mathbf{n}}$ will be discussed in subsection III.B). Note that frame $\mathcal{P}$ rotates at a *non-uniform* angular velocity about the z-axis, ω, due to the eccentricity of the orbits of the stars. Furthermore, frame $\mathcal{P}$ pulsates, i.e., it contracts and expands, such that α-Cen A and B are stationary along the x-axis. A *non-pulsating* synodic reference frame $\mathcal{NP}(\hat{\mathbf{x}}_{np}, \hat{\mathbf{y}}_{np}, \hat{\mathbf{z}}_{np})$ can also be defined, for which the direction of the axes are aligned with that of the pulsating frame, but the non-pulsating frame does not contract or expand. As a result, the location of α-Cen A and B along the x_{np}-axis varies with the true anomaly, θ, of the α-Cen AB system. A vector in the pulsating synodic reference frame, $\mathbf{s}_p$, can be transformed to a vector in the non-pulsating synodic reference frame, $\mathbf{s}_{np}$, via:

$$\mathbf{s}_{np} = \rho \mathbf{s}_p, \quad \rho = \frac{1 - e^2}{1 + e \cos \theta} \tag{1}$$

Note that, for $\theta = 0$ frames $\mathcal{P}$ and $\mathcal{NP}$ coincide. In frame $\mathcal{P}$, the equations of motion of the photon sail can be defined as [11, 23]:

$$x'' - 2y' = \frac{1}{1 + e \cos \theta} \left(\frac{\partial U}{\partial x} + a_{s,x} \right) \tag{2}$$

$$y'' + 2x' = \frac{1}{1 + e \cos \theta} \left(\frac{\partial U}{\partial y} + a_{s,y} \right) \tag{3}$$

5

$$z'' + z = \frac{1}{1 + e\cos\theta}\left(\frac{\partial U}{\partial z} + a_{s,z}\right) \tag{4}$$

where differentiation occurs with respect to the true anomaly. Furthermore, U is the effective potential that combines the gravitational and centripetal potentials, and $\mathbf{a}_s = [a_{s,x} \quad a_{s,y} \quad a_{s,z}]^\mathsf{T}$ is the acceleration induced by the photon sail. The latter will be discussed in detail in subsection III.B. Note that the equations of motion are made dimensionless by using the sum of the masses of α-Cen A and B, the instantaneous distance between the two stars and the inverse of the system's mean motion as the units of mass, distance, and time, respectively. As a result, the dimensionless mass of α-Cen B is given as $\mu = \frac{M_B}{M_A + M_B} = 0.4588$; one orbital period of the α-Cen AB system is represented by 2π; and the dimensionless position vectors of α-Cen A and B in frame $\mathcal{P}$ are given as $\mathbf{r}_A = [x + \mu \quad 0 \quad 0]^\mathsf{T}$ and $\mathbf{r}_B = [x - (1 - \mu) \quad 0 \quad 0]^\mathsf{T}$. The effective potential, U, can then be defined as $U = \frac{1}{2}\left(x^2 + y^2 + z^2\right) + \frac{1-\mu}{\|\mathbf{r}_A\|} + \frac{\mu}{\|\mathbf{r}_B\|}$.

B. Photon-pressure acceleration

Due to the presence of two radiative sources, the photon-sail acceleration in the α-Cen AB system, $\mathbf{a}_s$, is composed of two components, namely one component produced by α-Cen A, $\mathbf{a}_{s,A}$, and another component produced by α-Cen B, $\mathbf{a}_{s,B}$: $\mathbf{a}_s = \mathbf{a}_{s,A} + \mathbf{a}_{s,B}$. To further express these accelerations, an ideal reflectance model is adopted, which assumes perfect specular optical properties of the sail membrane and a flat, wrinkle-free surface. As a result, the photon-pressure acceleration will act normal to the sail surface, away from the radiating star [5]. While a conventional sail configuration has a reflective coating on only one side of the membrane and a high-emissivity coating on the other side (for thermal reasons), the derivation of the photon-pressure acceleration will initially assume a sail configuration where both sides of the sail membrane are reflective and are allowed to be illuminated (referred to as a two-sided sail). To define the direction of the vector normal to the sail surface (in short, the normal vector), two additional reference frames are introduced, $\mathcal{A}(\hat{\mathbf{r}}_A, \hat{\boldsymbol{\theta}}_A, \hat{\boldsymbol{\phi}}_A)$ and $\mathcal{B}(\hat{\mathbf{r}}_B, \hat{\boldsymbol{\theta}}_B, \hat{\boldsymbol{\phi}}_B)$, see Fig. 4, where:

$$\left(\hat{\mathbf{r}}_i = \frac{\mathbf{r}_i}{\|\mathbf{r}_i\|}, \quad \hat{\boldsymbol{\theta}}_i = \frac{\hat{\mathbf{z}} \times \hat{\mathbf{r}}_i}{\|\hat{\mathbf{z}} \times \hat{\mathbf{r}}_i\|}, \quad \hat{\boldsymbol{\phi}}_i = \frac{\hat{\mathbf{r}}_i \times \hat{\boldsymbol{\theta}}_i}{\|\hat{\mathbf{r}}_i \times \hat{\boldsymbol{\theta}}_i\|}\right), \quad i = A, B \tag{5}$$

The normal vector can be defined in both reference frames as:

$$\hat{\mathbf{n}}_i = \left(\cos\alpha_i \quad \sin\alpha_i \sin\delta_i \quad \sin\alpha_i \cos\delta_i\right)^\mathsf{T}, \quad i = A, B \tag{6}$$

where α_i and δ_i are the cone and clock angles, respectively, see Fig. 4b for their definition. With the definition of the normal vector as in Eq. 6, the dimensionless photon-sail acceleration can be defined as:

$$\mathbf{a}_s = \beta_A \frac{1-\mu}{\|\mathbf{r}_A\|^2} (\hat{\mathbf{r}}_A \cdot \hat{\mathbf{n}}_A)^2 \hat{\mathbf{n}}_A + \beta_B \frac{\mu}{\|\mathbf{r}_B\|^2} (\hat{\mathbf{r}}_B \cdot \hat{\mathbf{n}}_B)^2 \hat{\mathbf{n}}_B \tag{7}$$
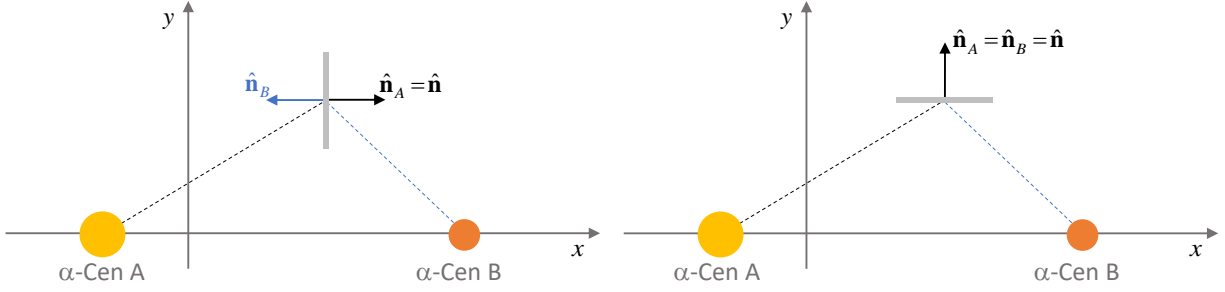
6

Fig. 5   Orientation of normal vectors $\hat{\mathbf{n}}_A$ and $\hat{\mathbf{n}}_B$ for a two-sided sail.

The definition in Eq. 7 largely follows the definition in Reference [5], but accounts for the luminosity and mass of the stars of the α-Cen AB system in the lightness numbers, β_i with $i = A, B$. The lightness number is defined as the ratio of the stellar radiation pressure acceleration and the stellar gravitational acceleration and is therefore independent of the distance to the star. Realistic lightness numbers reach up to $\beta_\odot = 0.04$ [24], while the Breakthrough Starshot project [25] and other studies into interstellar travel [8] assume much greater lightness numbers in the range 0.7 - 1779 by using gold foil and graphene for the sail membrane. Such large values for $\beta_\odot$ are required in order to enable travel to Alpha Centauri within a lifetime. Note that the subscript "$\odot$" in $\beta_\odot$ indicates that the lightness number is defined with respect to our own Sun. For the stars of the α-Cen AB system, the lightness number scales as $\beta_A = \epsilon_A \beta_\odot$ and $\beta_B = \epsilon_B \beta_\odot$ with $\epsilon_i = \frac{L_i M_\odot}{L_\odot M_i}$ and $i = A, B$, where L_i and M_i are the star's luminosity and mass as defined in Table 1. As an example, for $\beta_\odot = 1$, it follows that $\beta_A = 1.374$ and $\beta_B = 0.534$, indicating that the same sail performs 1.374 times better under the effect of α-Cen A and only 0.534 as well under the effect of α-Cen B. Important to note is that the photon-sail acceleration cannot be directed towards the respective star, i.e.:

$$(\hat{\mathbf{r}}_A \cdot \hat{\mathbf{n}}_A) \geq 0 \quad \text{and} \quad (\hat{\mathbf{r}}_B \cdot \hat{\mathbf{n}}_B) \geq 0 \tag{8}$$

or, alternatively, using the cone angle: $-90° \leq \alpha_A \leq 90°$ and $-90° \leq \alpha_B \leq 90°$. For a one-sided sail, a violation of the constraints in Eq. 8 would cause the highly emissive backside of the sail to be exposed to either of the stars, causing thermal control issues.

To simplify the expression in Eq. 7 and write the equation in a form suitable for analyses in the subsequent sections, the normal vector $\hat{\mathbf{n}}_A$ is defined as the reference normal direction, $\hat{\mathbf{n}}$. Then, once again considering the assumption of a two-sided sail, the normal vector $\hat{\mathbf{n}}_B$ can be expressed as:

$$\hat{\mathbf{n}}_B = \hat{\mathbf{n}} \quad \text{if } (\hat{\mathbf{r}}_B \cdot \hat{\mathbf{n}}) \geq 0$$
$$\hat{\mathbf{n}}_B = -\hat{\mathbf{n}} \quad \text{otherwise} \tag{9}$$

7

Both cases in Eq. 9 are illustrated in Fig. 5, where it is shown that the bottom equation in Eq. 9 flips the normal vector away from α-Cen B when one side of the sail is illuminated by α-Cen A and the other side by α-Cen B (see the illustration on the right). Substituting the expression for the scaled lightness number and Eq. 9 into Eq. 7 yields:

$$\mathbf{a}_s = \beta_\odot \left(\epsilon_A \frac{1-\mu}{\|\mathbf{r}_A\|^2} \left(\hat{\mathbf{r}}_A \cdot \hat{\mathbf{n}} \right)^2 + u \epsilon_B \frac{\mu}{\|\mathbf{r}_B\|^2} \left(\hat{\mathbf{r}}_B \cdot \hat{\mathbf{n}} \right)^2 \right) \hat{\mathbf{n}} \tag{10}$$

with

$$u = 1 \quad \text{if } (\hat{\mathbf{r}}_B \cdot \hat{\mathbf{n}}) \geq 0$$
$$u = -1 \quad \text{if } (\hat{\mathbf{r}}_B \cdot \hat{\mathbf{n}}) < 0 \text{ and for a two-sided sail only} \tag{11}$$

The bottom row in Eq. 11 specifically adds the condition of a two-sided sail such that Eqs. 10 and 11, together with the constraints in Eq. 8 define the photon-sail acceleration experienced by both a one-sided and a two-sided sail in the α-Cen AB system. Recall that, for a one-sided sail, only the reflective side of the sail can be illuminated by both stars, implying that $\hat{\mathbf{n}}_A$ and $\hat{\mathbf{n}}_B$ should always be aligned and cannot be directed opposite to one another. Therefore, the situation on the right-hand side of Fig. 5 cannot occur and presents an infeasible situation for a one-sided sail as in that case $\hat{\mathbf{n}}_B = \hat{\mathbf{n}}$, which would violate the second constraint in Eq. 8.

IV. Equilibria

The addition of a photon-sail acceleration to any three-body system enables the displacement of the five classical equilibria or Lagrange points, resulting in so-called artificial equilibria (AE). AE have been investigated extensively in the dynamics of our own Solar System, and particularly in the framework of the *circular* restricted three-body problem (see, for example Reference [5]). Artificial equilibria and orbits around them in either the ER3BP [11–14] or under the effect of two radiative sources [10, 26] have been investigated to lesser extent. Regarding the ER3BP, it is known from the literature [11] that such artificial equilibria only exist in the (x, y)-plane due to the incommensurability in pulsation between the motion in the (x, y)-plane and the motion in $\hat{\mathbf{z}}$-direction. To obtain the AE in the (x, y)-plane from Eqs. 2-4, all derivatives with respect to the true anomaly are set to zero and $z = 0$ is substituted. The required photon-sail acceleration to convert an arbitrary location in frame $\mathcal{P}$ into an equilibrium, can then be derived in vector form as $\mathbf{a}_s = -\nabla U$. Because the vector ∇U coincides with the (x, y)-plane due to $z = 0$, the photon-sail acceleration vector also coincides with the (x, y)-plane. The clock angle of the photon sail therefore equals $\delta_i = 0.5\pi$. To obtain the required orientation of the sail, i.e., the normal vector, $\hat{\mathbf{n}}$, and the required performance of the sail, i.e., the lightness number, $\beta_\odot$, the approach in Reference [5] is adopted. First, to obtain the required orientation of the sail, the vector product of $\mathbf{a}_s = -\nabla U$ with $\hat{\mathbf{n}}$ is taken to yield $\hat{\mathbf{n}} = -\frac{\nabla U}{\|\nabla U\|}$. This expression shows that an equilibrium solution is found when the sail's normal vector is directed opposite to the gradient of the effective potential. To obtain the required
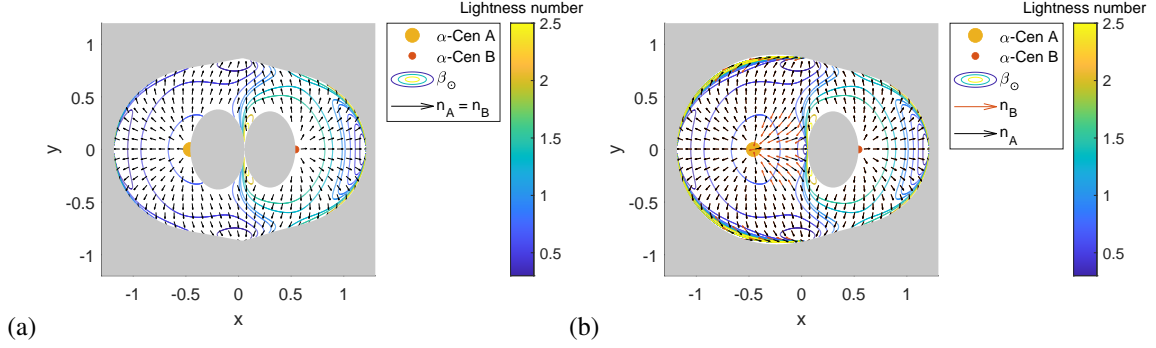
8

Fig. 6 **Lightness number contours for** $\beta_\odot$=[0.3 0.5 0.7 0.9 1 1.3 1.5 2 2.5]. **a) one-sided sail. b) two-sided sail.**

ligthness number, the dot product of $\mathbf{a}_s = -\nabla U$ with $\hat{\mathbf{n}}$ is taken to yield:

$$\beta_\odot = \frac{-\nabla U \cdot \hat{\mathbf{n}}}{\epsilon_A \frac{1-\mu}{||\mathbf{r}_A||^2} \left(\hat{\mathbf{r}}_A \cdot \hat{\mathbf{n}}\right)^2 + u\epsilon_B \frac{\mu}{||\mathbf{r}_B||^2} \left(\hat{\mathbf{r}}_B \cdot \hat{\mathbf{n}}\right)^2} \tag{12}$$

As both expressions for the normal vector and lightness number only depend on the position coordinates, contours of equal lightness number can be drawn in the (x, y)-plane as shown in Fig. 6 for a one-sided and two-sided sail, respectively. In these figures, grey-shaded areas indicate regions of infeasiblity where one or both constraints in Eq. 8 are not met. Arrows indicate the required direction of the sail normal vectors, $\hat{\mathbf{n}}_A$ and $\hat{\mathbf{n}}_B$. Note that, for the one-sided sail in Fig. 6a, both normal vectors are aligned, whereas for the two-sided sail in the right plot regions exist where the condition in the bottom row of Eq. 11 applies and $\hat{\mathbf{n}}_B$ is oriented opposite to $\hat{\mathbf{n}}_A$. From comparing Fig. 6a and Fig. 6b it is clear that a two-sided sail makes regions of AE accessible that are not accessible by the one-sided sail. For example, when observing the left infeasible region in between α-Cen A and B for the one-sided sail, it can be concluded that this infeasibility is caused by the fact that the required sail normal vector (black arrows) points towards α-Cen B. Due to the two-sided reflective nature of the sail in the right plot of Fig. 6, the normal vector with respect to α-Cen B can be "flipped" (red arrows), making this region accessible to the two-sided sail and allowing the sail to be situated in between α-Cen A and B. A similar reasoning holds for the outer edges of the region of AE for negative values of x.

To show the effect of the additional radiative source in a *binary*-star system, Fig. 7 is added that presents the results for a one-sided sail in the hypothetical case that the luminosity of α-Cen B is set to zero. While the contours on the left-hand side of Fig. 7, i.e., around α-Cen A, do not change much with respect to those in Fig. 6, the effect of the luminosity of α-Cen B on the contours of equilibria around α-Cen B is evident: the photon-sail acceleration generated by α-Cen B in the binary-star system allows equilibria to exist much closer to α-Cen B and for much smaller lightness numbers than when α-Cen B would be non-radiative.

It is important to note that the equilibria found in this section are only stationary points in the pulsating frame, i.e.,
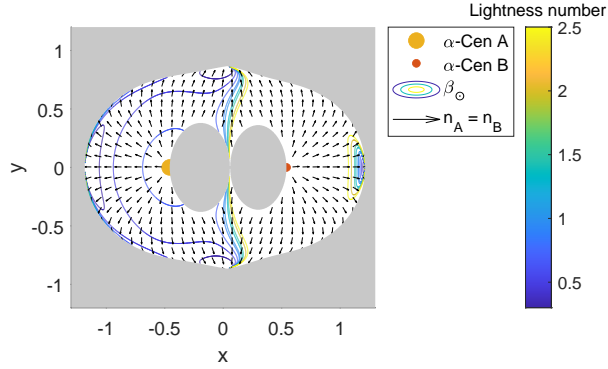
Fig. 7   Zero-luminosity for α-Cen B and one-sided sail: lightness number contours for $\beta_\odot$=[0.3 0.5 0.7 0.9 1 1.3 1.5 2 2.5].

with respect to the true anomaly. Instead, in the non-pulsating synodic reference frame, $\mathcal{NP}$, they trace out periodic trajectories [23]. To show how the location of the equilibria indeed changes over time, Fig. 8 is included where the lightness number contours for a one-sided sail are translated to the non-pulsating synodic reference frame. Figure 8a-c shows this change over one orbital evolution of the α-Cen AB system through three values for the true anomaly, $\theta = 0$, 90 deg and 180 deg. Note that, due to the periodicity of the dynamics for $\theta = 270$ deg, the same results as in Fig. 8b would be obtained. Though, over time, the contours do not change in a qualitative sense, they do change in size as they contract and expand as a function of θ (note the different scales on the axes). To illustrate the extent to which the equilibria migrate over time even better, Fig. 8d is added, which presents the contour for $\beta_\odot = 0.7$ and the region of infeasibility (RoI) at $\theta = 0$ deg as well as the location of α-Cen A, α-Cen B and one arbitrarily chosen AE along the $\beta_\odot$ = 0.7 contour for a stepwise increase in θ from 0 deg to 180 deg. The arrows connected to the AE once again indicate the required sail normal vector, i.e., $\hat{\mathbf{n}} = \hat{\mathbf{n}}_A = \hat{\mathbf{n}}_B$. Note that, for the second half of the orbital revolution of the α-Cen AB system (i.e., for $\theta = 180$ to 360 deg), the reverse of the motion as shown in Fig. 8d would be observed to obtain a periodic trajectory in the non-pulsating synodic reference frame.

As a final note, it should be mentioned that the accessibility of the equilibria found in this section after interstellar travel from Earth to Alpha Centauri is beyond the scope of this work. However, trajectories that allow deceleration and capture into the Alpha-Centauri system have been developed [8, 27] and give confidence in the photon-sail's ability to target the equilibria for a wide range of lightness numbers; only the allowable entry speed into the Alpha-Centauri system, and therefore the transit time from Earth to Alpha Centauri, is affected by the lightness number, where larger lightness numbers (and hence larger entry speeds) allow faster transits from Earth to Alpha Centauri.

V. Stability of Equilibria

To determine the stability of the equilibria derived in the previous section, this section follows the approach in Reference [11]. There, the stability of an equilibrium is determined through the eigenvalues of the monodromy matrix
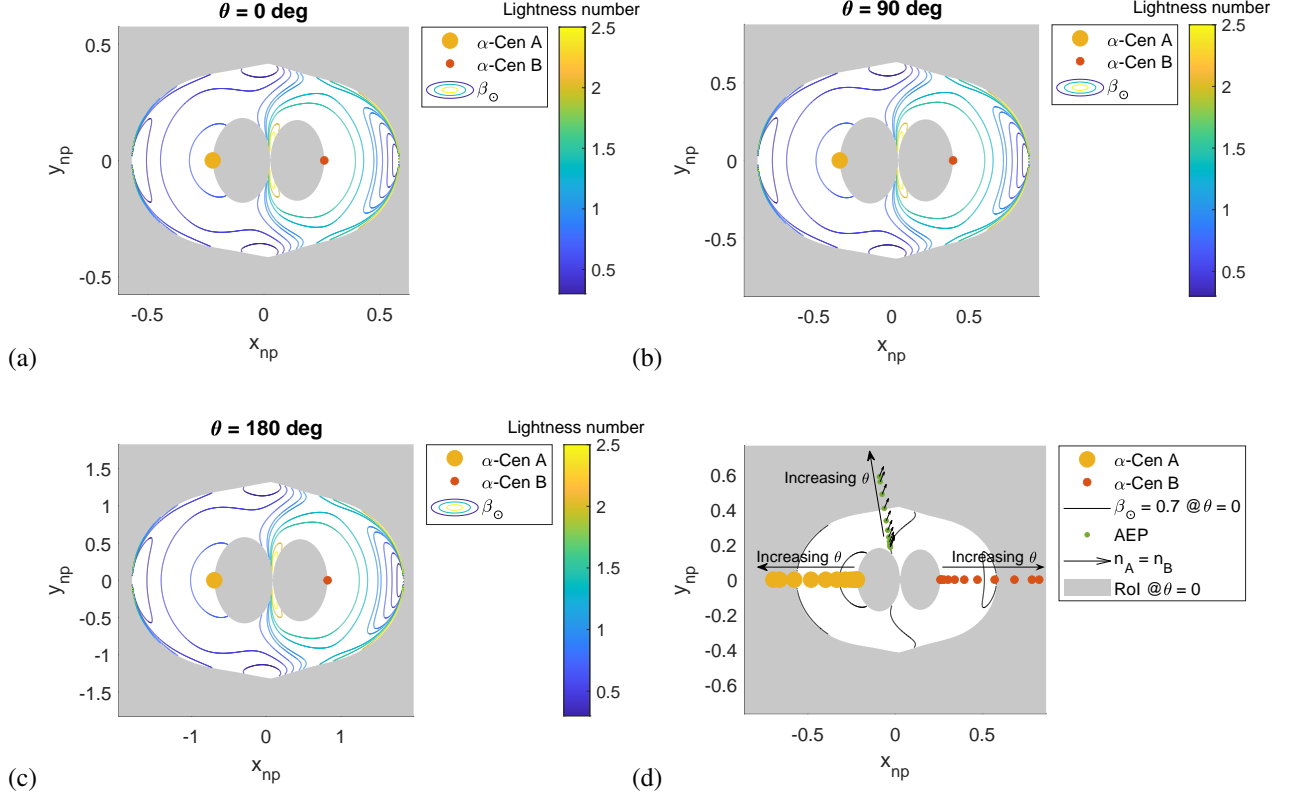
Fig. 8 **One-sided sail. a-c) Evolution of lightness number contours in frame $\mathcal{NP}$ for $\beta_\odot$=[0.3 0.5 0.7 0.9 1 1.3 1.5 2 2.5]. d) Evolution of a single AE for $\beta_\odot = 0.7$.**

which is the state transition matrix, $\Phi(\theta; \theta_0)$, evaluated after one period of the system, i.e., $\Phi(\theta_0 + 2\pi, \theta_0)$. To obtain the state transition matrix, the dynamical system in Eqs. 2-3 is linearized around the equilibrium, $\mathbf{R}_0 = [x_0 \quad y_0]$ that can be maintained through a sail attitude defined by $\hat{\mathbf{n}}_0 = \hat{\mathbf{n}}$. Note that, as equilibria only exist in the (x, y)-plane, the analysis in this section is also reduced to two-dimensional form. By applying a small perturbation, $\mathbf{R} \rightarrow \mathbf{R}_0 + \delta\mathbf{R}$, a linearized system of first-order differential equations in the form of $\mathbf{X}' = A\mathbf{X}$ is obtained with $\mathbf{X} = [\delta\mathbf{R} \quad \delta\mathbf{R}']$ and

$$A = \begin{bmatrix} 0 & I|_{2\times 2} \\ \frac{K}{1+e\cos(\theta)} & S \end{bmatrix} \quad , \quad K = \left(\frac{\partial \nabla U}{\partial \mathbf{R}} + \frac{\partial \mathbf{a}_s}{\partial \mathbf{R}} \right)\Bigg|_{\mathbf{R}_0, \hat{\mathbf{n}}_0} \quad , \quad S = \begin{bmatrix} 0 & 2 \\ -2 & 0 \end{bmatrix} \quad , \quad I|_{2\times 2} = \begin{bmatrix} 1 & 0 \\ 0 & 1 \end{bmatrix} \quad (13)$$

Note that the matrix K is evaluated at the equilibrium point, keeping both the position vector and sail attitude constant and equal to their values at the equilibrium, $\mathbf{R}_0$ and $\hat{\mathbf{n}}_0$, respectively. For the linearized system, the state transition matrix $\Phi(\theta; \theta_0)$ can be obtained from a numerical propagation of the following set of first order differential equations: $\Phi'(\theta; \theta_0) = A\Phi(\theta; \theta_0)$. In particular, starting from the initial condition $\Phi(0; 0) = I|_{4\times 4}$ and integrating from $\theta_0 = 0$ to $\theta = 2\pi$ yields the monodromy matrix, whose eigenvalues characterize the linear stability of the equilibrium. If the
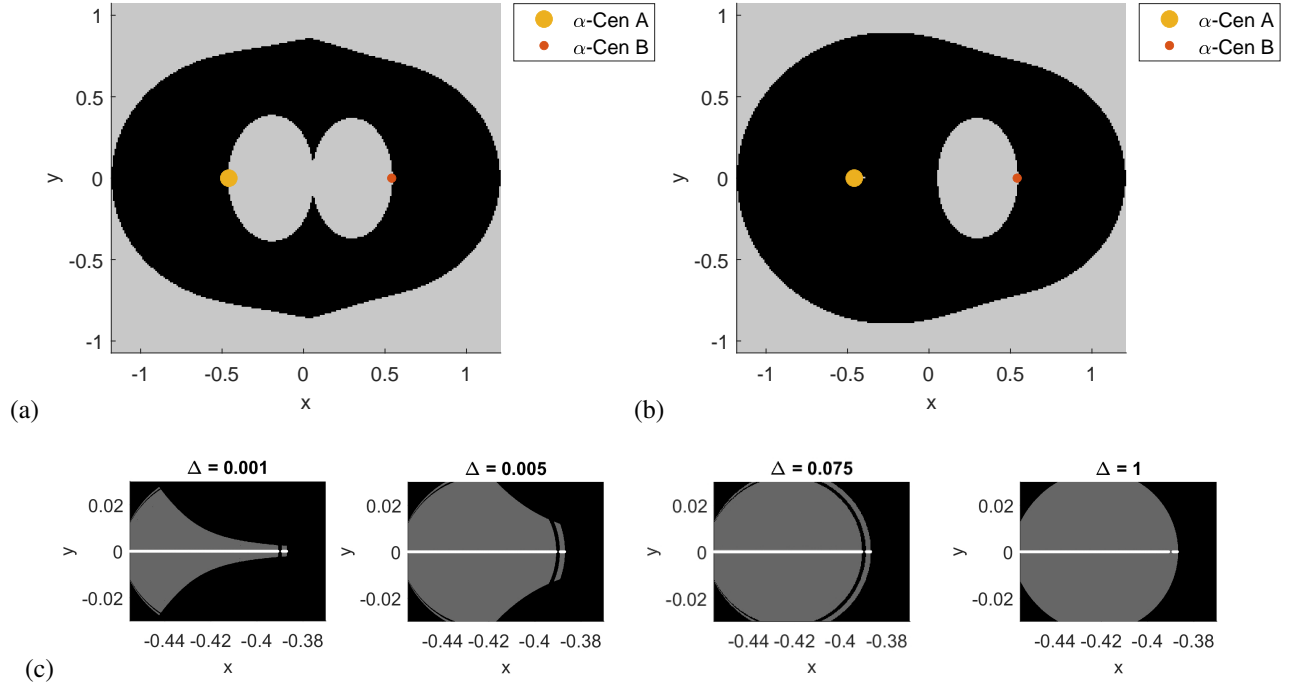
Fig. 9 a-c) Linear stability of equilibria; black, dark-gray, white and light-gray shaded areas indicate instability, almost-stability, stability and infeasibility, respectively. a) One-sided sail. b) Two-sided sail. c) Close-up for two-sided sail for different values for Δ in the definition of almost-stability.

eigenvalues, λ_i, of the monodromy matrix satisfy $|\lambda_i| \leq 1$ [11], the system is linearly stable; if $|\lambda_i| \leq 1 + \Delta$ the system is said to be almost stable, where Δ is a small number; otherwise it is linearly unstable. To integrate the system of differential equations, the *ode45* integrator in MATLAB® is employed with relative and absolute tolerances of 10^{-12}. The results are shown in Fig. 9 for both a one-sided and a two-sided sail. Black, dark-gray and white shaded areas indicate regions of unstable, almost-stable and stable equilibria, respectively, while light-gray shaded areas indicate infeasibility similar to the figures in Section IV. The top row provides a system-wide overview, showing that the majority of the equilibria are unstable, except for a very small region close to α-Cen A for a two-sided sail. A close-up of that region for different values for Δ is provided in Fig. 9c. The existence of stable equilibria along the line connecting the two stars indicates that the spacecraft may maintain a position in between α-Cen A and B with minimum orbit control while allowing to observe both stars simultaneously. Though the almost-stable equilibria in the dark-gray shaded regions will require more orbit control, the fact that their eigenvalues are only slightly larger than unity implies that the spacecraft will naturally leave the equilibrium only after a relatively long period of time.
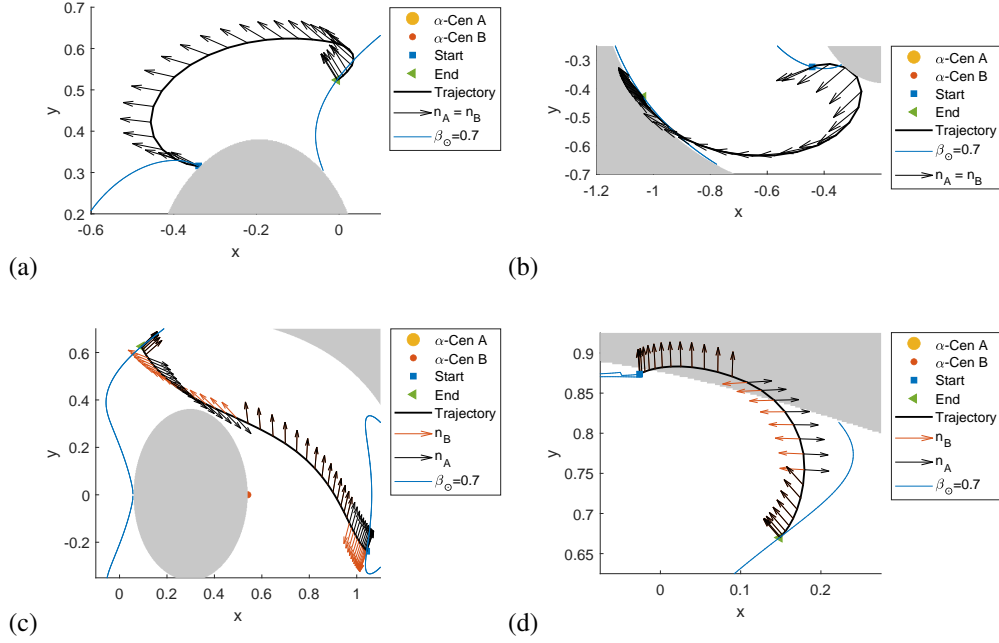
Fig. 10   Motion between artificial equilibria. For further transfer details, see Table 3. a) Transfer 1. b) Transfer 2. c) Transfer 3. d) Transfer 4.

VI. Motion between Equilibria

The results in Fig. 9 may seed many new avenues for future exploration of the dynamics of a photon-sail in the α-Cen AB system, including heteroclinic-like connections between the equilibria. Here, a heteroclinic-like connection refers to the photon-sail enabled motion between equilibria that belong to different contours but exist for equal lightness number. As a case study, this section investigates motion between AE on contours for $\beta_\odot = 0.7$. These contours appear as blue solid lines in Fig. 10 for both the one- (top row) and two-sided (bottom row) sail configurations. Two contour arcs (from here on referred to as the departure and arrival arcs) are selected to move between, where each arc comprises hundreds of equilibria. Subsequently, a piecewise constant sail attitude along two trajectory segments is assumed. The first trajectory segment is generated by a forwards propagation of the dynamics in Eqs. 2-3 from $\theta = 0$ and from a to-be-selected equilibrium point, E_d, along the departure arc with state vector $\mathbf{x}_{d,0}$ while using a piecewise constant sail attitude described by a sequence of cone angles $\boldsymbol{\alpha}_d = [\alpha_{d,1} \quad \alpha_{d,2} \quad ...]$. The second trajectory segment is obtained by a backwards propagation from a to-be-selected equilibrium point, E_a, along the arrival arc with state vector $\mathbf{x}_{a,0}$, again using a piecewise constant sail attitude described by $\boldsymbol{\alpha}_a = [\alpha_{a,1} \quad \alpha_{a,2} \quad ...]$. Note that these cone angles describe the orientation of the sail normal vector with respect to α-Cen A, i.e., they define $\hat{\mathbf{n}}$ in Eq. 10. The amount of time (expressed in true anomaly) that each sail attitude is maintained is denoted by $\boldsymbol{\theta}_\alpha = [\theta_{d,1} \quad \theta_{d,2} \quad ... \quad \theta_{a,1} \quad \theta_{a,2} \quad ...]$, where the subscripts correspond to the subscripts of the cone-angle notation. The state vectors at the end of the forwards and backwards propagated trajectory segments are denoted as $\mathbf{x}_{d,f}$ and $\mathbf{x}_{a,f}$, respectively. The problem then becomes of

13

finding values for the decision vector $\mathbf{y} = [E_d \quad E_a \quad \alpha_d \quad \alpha_a \quad \theta_\alpha]$ that allows a connection in phase space between the departure and arrival trajectory segments. To find those values, a genetic algorithm implemented in the MATLAB® *ga.m* function is employed. The cost function of the genetic algorithm is set to the minimum Euclidean norm between the end of the departure trajectory segment and the start of the arrival trajectory segment: $J = \|\mathbf{x}_{d,f} - \mathbf{x}_{a,f}\|$. Bounds on the decision vector are defined as follows:

$$\begin{bmatrix} 1 & 1 & -\frac{1}{2}\pi & -\frac{1}{2}\pi & 0.02\pi \end{bmatrix} \leq \mathbf{y} = [E_d \quad E_a \quad \alpha_d \quad \alpha_a \quad \theta_\alpha] \leq \begin{bmatrix} E_{d,max} & E_{a,max} & \frac{1}{2}\pi & \frac{1}{2}\pi & \theta_{\alpha,max} \end{bmatrix}$$

(14)

where $E_{d,max}$ and $E_{a,max}$ represent the number of equilibria along each contour arc, while $\theta_{\alpha,max}$ represents the maximum duration that each sail attitude is maintained.

As a preliminary demonstration that motion between equilibria is theoretically feasible, four transfers have been investigated; two for a one-sided sail and two for a two-sided sail. The results appear in Fig. 10 and Table 3, where the table also provides further details on $E_{d,max}$, $E_{a,max}$ and $\theta_{\alpha,max}$. For each transfer, the algorithm is run for five different seed values to account for the inherent randomness in the genetic-algorithm approach and a population size of 500 and a maximum number of generations of 200 is used. For all other settings of the genetic algorithm, the default settings of the *ga.m* implementation are adopted.

From test runs it appeared that two different sail attitudes in the departure trajectory and one sail attitude in the arrival trajectory provided suitable results in terms of objective function value, see also the columns for α_d and α_a in Table 3. The obtained objective function values, ranging from approximately 5×10^{-5} to 10^{-4} in dimensionless value, are similar to those obtained for other photon-sail enabled heteroclinic-like connections in three-body problems that also employed a methodology based on genetic algorithms [28, 29]. When summing the duration that each sail attitude is maintained, i.e., summing the elements of the $\theta_{\alpha,max}$ vector in Table 3, the total duration of the transfers considered ranges from 0.79π to 1.92π, i.e., up to a maximum of one α-Cen "year", which is equal to almost 80 Earth years, see Table 2.

Though these trajectories are not truly feasible due to the remaining error in position and velocity at the linkage of the departure and arrival trajectory segments, they do provide a first insight into the possibility of motion between AE in the α-Cen AB system. Using the obtained trajectory as an initial guess for more advanced numerical methods, such as multiple shooting differential correction, or even optimization methods, will allow more frequent and smoother sail attitude changes along the trajectory. Such an approach has already been demonstrated to be successful for finding photon-sail heteroclinic-like connections in and between a range of Sun-planet systems [15–17] for linkage errors of similar magnitude and may therefore also allow finding feasible and potentially time-optimal transfers in the α-Cen AB system.

Table 3 Details of the transfers in Fig. 10. The errors in position and velocity are in dimensionless units.

Transfer number	Reflective	$E_{d,max}$	$E_{a,max}$	$\theta_{\alpha,max}$	α_d, deg	α_a, deg	θ_α	J	Dimension-less error in position	Dimension-less error in velocity
1	One-side	674	423	$\begin{bmatrix}1\\1\\1\end{bmatrix}\pi$	$\begin{bmatrix}84\\89\end{bmatrix}$	73	$\begin{bmatrix}0.90\\0.28\\0.20\end{bmatrix}\pi$	1.3×10^{-4}	1.0×10^{-4}	2.4×10^{-5}
2	One-side	674	507	$\begin{bmatrix}1\\1\\1\end{bmatrix}\pi$	$\begin{bmatrix}-72\\-82\end{bmatrix}$	-87	$\begin{bmatrix}0.52\\0.64\\0.76\end{bmatrix}\pi$	4.7×10^{-5}	3.3×10^{-5}	1.4×10^{-5}
3	Two-side	835	622	$\begin{bmatrix}\frac12\\\frac12\\\frac12\end{bmatrix}\pi$	$\begin{bmatrix}80\\-66\end{bmatrix}$	-5	$\begin{bmatrix}0.48\\0.24\\0.10\end{bmatrix}\pi$	4.6×10^{-5}	3.4×10^{-5}	1.2×10^{-5}
4	Two-side	1930	622	$\begin{bmatrix}\frac12\\\frac12\\\frac12\end{bmatrix}\pi$	$\begin{bmatrix}30\\-53\end{bmatrix}$	83	$\begin{bmatrix}0.34\\0.20\\0.24\end{bmatrix}\pi$	1.1×10^{-4}	1.0×10^{-4}	5.0×10^{-6}

VII. Conclusion

This Note has investigated the photon-sail orbital dynamics in the Alpha-Centauri system. In particular, the orbital dynamics in the binary-star system consisting of the stars α-Cen A and α-Cen B has been explored. A new photon-sail acceleration model for a sail membrane that is reflective on either one side or on both sides is derived and conveniently expressed as a function of the photon-sail lightness number with respect to our own Sun while correcting for the different masses and luminosities of α-Cen A and B. By augmenting the elliptic restricted three-body problem (consisting of the stars α-Cen A and B and the photon-sail spacecraft), new equilibria have come to light with respect to equilibria known to exist in single-star systems such as our own Sun-Earth system. In particular, the photon-sail acceleration generated by the secondary star, α-Cen B, allows equilibria to exist much closer to the smaller primary, i.e., α-Cen B, and for much smaller lightness numbers than when α-Cen B would be non-radiative. The majority of these equilibria are unstable, except for a very small region of linearly stable and almost-stable equilibria close to α-Cen A for a two-sided sail. Finally, motion between equilibria belonging to different contours but for the same lightness number has been proven feasible, though the adopted approach leaves an error in position and velocity at the linkage of two trajectory segments: one segment departing from the initial equilibrium and one segment arriving at the final equilibrium. However, these errors may be small enough for the obtained transfers to serve as a first guess for more advanced numerical methods and as such do not detract from the insight that these transfers provide into the possibility of motion between equilibria in the α-Cen AB system.

References

[1] Kervella, P., and Thévenin, F., "A Family Portrait of the Alpha Centauri System," , 2003. URL https://www.eso.org/

`public/news/eso0307/`, [retrieved 5 June 2020], European Southern Observatory (Release No. eso0307, Legacy ID PR 05/03).

[2] Pino, T., and Circi, C., "A star-photon sailcraft mission in the Alpha Centauri system," *Advances in Space Research*, Vol. 59, 2017, pp. 2389 – 2397. doi:10.1016/j.asr.2017.02.014.

[3] Anglada-Escudé, G., Amado, P. J., Barnes, J., Berdiñas, Zaira M., Butler, R. Paul, Coleman, Gavin A. L., de la Cueva, Ignacio, Dreizler, Stefan, Endl, Michael, Giesers, Benjamin, Jeffers, Sandra V., Jenkins, James S., Jones, Hugh R. A., Kiraga, Marcin, Kürster, Martin, López-González, María J., Marvin, Christopher J., Morales, Nicolás, Morin, Julien, Nelson, Richard P., Ortiz, José L., Ofir, Aviv, Paardekooper, Sijme-Jan, Reiners, Ansgar, Rodríguez, Eloy, Rodríguez-López, Cristina, Sarmiento, Luis F., Strachan, John P., Tsapras, Yiannis, Tuomi, Mikko, and Zechmeister, Mathias, "A terrestrial planet candidate in a temperate orbit around Proxima Centauri," *Nature*, Vol. 536, 2016, pp. 437–440. doi:10.1038/nature19106.

[4] Macdonald, M., and McInnes, C., "Solar Sail Science Mission Applications and Advancement," *Advances in Space Research*, Vol. 48, No. 11, 2011, pp. 1702–1716. doi:10.1016/j.asr.2011.03.018.

[5] McInnes, C. R., *Solar Sailing: Technology, Dynamics and Mission Applications*, Springer - Praxis Books in Astronautical Engineering, Springer-Verlag, Berlin, Germany, 1999, pp. 1, 214–224.

[6] Russell Lockett, T., Johnson, C., Few, A., and Stewart, E., "Lessons Learned from the Flight Unit Testing of the Near Earth Asteroid Scout Flight System," *Fifth International Symposium on Solar Sailing*, 2019.

[7] Leipold, M., Fichtner, H., Heber, B., Groepper, P., Lascar, S., Burger, F., Eiden, M., Niederstadt, T., Sickinger, C., Herbeck, L., Dachwald, B., and Seboldt, W., "Heliopause Explorer - A Sailcraft Mission to the Outer Boundaries of the Solar System," *Acta Astronautica*, Vol. 59, 2006, pp. 785–796. doi:10.1016/j.actaastro.2005.07.024.

[8] Heller, R., and Hippke, M., "Deceleration of High-velocity Interstellar Photon Sails into Bound Orbits at α Centauri," *The Astrophysical Journal Letters*, Vol. 835, No. L32, 2017. doi:10.3847/2041-8213/835/2/L32.

[9] Heller, R., Hippke, M., and Kervella, P., "Optimized Trajectories to the Nearest Stars Using Lightweight High-velocity Photon Sails," *The Astronomical Journal*, Vol. 154, No. 115, 2017. doi:10.3847/1538-3881/aa813f.

[10] Aliasi, G., Mengali, G., and Quarta, A. A., "Artificial equilibrium points for a solar balloon in the α Centauri system," *Acta Astronautica*, Vol. 104, No. 2, 2014, pp. 464 – 471. doi:10.1016/j.actaastro.2014.03.006.

[11] Baoyin, H., and McInnes, C. R., "Solar Sail Equilibria in the Elliptical Restricted Three-Body Problem," *Journal of Guidance, Control and Dynamics*, Vol. 29, No. 3, 2006, pp. 538–543. doi:10.2514/1.15596.

[12] Aliasi, G., Mengali, G., and Quarta, A. A., "Artificial equilibrium points for a generalized sail in the elliptic restricted three-body problem," *Celestial Mechanics and Dynamical Astronomy*, Vol. 114, No. 1, 2012, pp. 181–200. doi:10.1007/s10569-012-9425-z, URL `https://doi.org/10.1007/s10569-012-9425-z`.

[13] Biggs, J., McInnes, C., and Waters, T., "Control of Solar Sail Periodic Orbits in the Elliptic Three-Body Problem," *Journal of Guidance, Control, and Dynamics*, Vol. 32, No. 1, 2009, pp. 318–320. doi:10.2514/1.38362.

[14] Gong, S., and Li, J., "Solar Sail Periodic Orbits in the Elliptic Restricted Three-Body Problem," *Celestial Mechanics and Dynamical Astronomy*, Vol. 121, No. 2, 2015, pp. 121–137. doi:10.1007/s10569-014-9590-3, URL `https://doi.org/10.1007/s10569-014-9590-3`.

[15] Farres, A., Heiligers, J., and Miguel Baños, N., "Road Map to L4/L5 with a solar sail," *28th AIAA/AAS Space Flight Mechanics Meeting*, Kissimmee, Florida, USA, 2018, p. 21. doi:10.2514/6.2018-0211.

[16] Vergaaij, M., and Heiligers, J., "Time-optimal solar sail heteroclinic-like connections for an Earth-Mars cycler," *Acta Astronautica*, Vol. 152, 2018, pp. 474–485. doi:10.1016/j.actaastro.2018.08.008.

[17] Heiligers, J., Fernandez Mora, A., Farrés, A., Miguel, N., and Wilkie, K., "Solar-Sail Pathways to the Sun-Earth L5 Point," *Fifth International Symposium on Solar Sailing*, Aachen, Germany, 2019.

[18] Kervella, P., Thévenin, F., and Lovis, C., "Proxima's orbit around α Centauri," *Astronomy and Astrophysics*, Vol. 598, No. L7, 2017. doi:10.1051/0004-6361/201629930.

[19] Argyle, R. W., *Observing and Measuring Visual Double Stars*, Springer Science & Business Media, 2012, Chap. The Orbital Elements of a Visual Binary Star, pp. 53–61.

[20] Murray, C. D., and Correia, A. C. M., *Exoplanets*, University of Arizona Press, Tucson, Arizona, USA, 2010, Chap. Keplerian Orbits and Dynamics of Exoplanets, pp. 15–23.

[21] Thévenin, F., Provost, J., Morel, P., Berthomieu, G., Bouchy, F., and Carrier, F., "Asteroseismology and calibration of α Cen binary system," *Astronomy and Astrophysics*, Vol. 392, No. 1, 2002, pp. L9–L12. doi:10.1051/0004-6361:20021074.

[22] Kervella, P., Mignard, F., Mérand, A., and Thévenin, F., "Close stellar conjunctions of α Centauri A and B until 2050 - An m_K = 7.8 star may enter the Einstein ring of α Cen A in 2028," *Astronomy and Astrophysics*, Vol. 594, 2016, p. A107. doi:10.1051/0004-6361/201629201.

[23] Szebehely, V., *Theory of Orbits: The Restricted Problem of Three Bodies*, Academic Press, 1967. doi:10.1016/B978-0-12-395732-0.50003-9.

[24] Heiligers, J., Fernandez, J., Stohlman, O., and Wilkie, K., "Trajectory Design for a Solar-Sail Mission to Asteroid 2016 HO3," *Astrodynamics*, Vol. 3, No. 3, 2019, pp. 231–246. doi:10.1007/s42064-019-0061-1.

[25] , 2020. URL `https://breakthroughinitiatives.org/initiative/3`.

[26] Narayan, A., and Singh, N., "Motion and stability of triangular equilibrium points in elliptical restricted three body problem under the radiating primaries," *Astrophysics and Space Science*, Vol. 352, No. 1, 2014, pp. 57–70. doi:10.1007/s10509-014-1903-1.

[27] Schoutetens, F., "Photon-Sail Trajectory Optimization in Alpha Centauri Using Evolutionary Neurocontrol," Msc thesis, 2019.

[28] Heiligers, J., "Homo- and Heteroclinic Connections in the Planar Solar-Sail Earth-Moon Three-Body Problem," *Frontiers in Applied Mathematics and Statistics*, 2018. doi:10.3389/fams.2018.00042.

[29] Vergaaij, M., and Heiligers, J., "Solar-Sail Trajectory Design to Planetary Pole Sitters," *Journal of Guidance, Control, and Dynamics*, Vol. 42, No. 6, 2019, pp. 1402–1412. doi:10.2514/1.g003952.